SCATTERED ENERGY INVERSION OF SEISMIC DATA

JEWOO YOO[1], WANSOO HA[2], CHANGSOO SHIN[2] and DONG-JOO MIN[2]

[1] *Department of Computational Science & Technology, Seoul National University, Seoul, South Korea.*
[2] *Department of Energy Systems Engineering, Seoul National University, Seoul, South Korea.*
wansooha@gmail.com

(Received April 27, 2012; revised version accepted February 26, 2013)

ABSTRACT

Yoo, J., Ha, W., Shin, C. and Min, D.-J., 2013. Scattered energy inversion of seismic data. *Journal of Seismic Exploration*, 22: 183-208.

We propose a new algorithm to build a macro-velocity model using scattered energy from a seismic signal. This method does not require an iterative procedure or an estimation of the source wavelet. Consequently, it is an inexpensive and efficient method to delineate a macro-velocity model. We acquire information concerning the velocity differences similar to a gravity or magnetic field and build a macro-velocity model. Thus, subsequent inversion in the time or frequency domains can recover structures with sharp velocity variations from the constructed velocity model as an initial velocity model.

KEY WORDS: scattering energy, velocity anomaly, Born theory, gravity inversion.

INTRODUCTION

Geophysicists study subsurface structures using information recorded at the surface in various ways, one of which is a full waveform inversion. However, recovering an accurate velocity model from field data or even synthetic data can be difficult due to local minima in the objective functions and the absence of low-frequency components in the data.

0963-0651/13/$5.00

These difficulties lead to the use of a two-step inversion process. In the first step, a large-scale velocity model is recovered, and in the second step, inversion is performed to improve the resolution of the velocity model. There are several methods that can be used to obtain a reliable macro-velocity model, such as traveltime tomography (Luo and Schuster, 1991; Chapman and Pratt, 1992) and inversion algorithms in the Laplace domain (Shin and Cha, 2008). Traveltime tomography reconstructs the subsurface velocity model by minimizing the residuals between the modeled and observed traveltimes (Luo and Schuster, 1991; Chapman and Pratt, 1992). However, its penetration depth can be prohibitively shallow, and the method relies on the arrival times chosen. The macro-velocity model can also be estimated by an inversion in the Laplace domain. The Laplace-domain inversion scheme has been shown to be successful in recovering reliable macro-velocity models from field data containing a small amount of low-frequency components (Shin and Cha, 2008; Shin and Ha, 2008). However, the Laplace-domain inversion suffers from noise appearing before the first arrival. Muting is therefore mandatory in Laplace-domain inversion.

In this study, we propose a new algorithm to recover macro-velocity models of the subsurface. Our study begins with the simple idea that the reflected waves from high-velocity structures have large amplitudes. We assumed a medium with a homogeneous density. Thus, we surmise that the energy computed from recorded data can be used to reveal high-velocity structures in the subsurface. This method is analogous to the gravity inversion method (Last and Kubik, 1983; Guspi, 1993). Furthermore, we assume that the energy of the observed seismogram is similar to a gravity anomaly in gravity inversion. Gravity anomalies from each subsurface structure are similar to the energy of perturbed signals from each scatterer.

In this study, we convert wavefield data to energy data to recover high-velocity anomalies. We assume that the wavefield data are the sum of scattered signals by point scatterers in the subsurface following the Born theory (Ikelle and Amundsen, 2005), and we build a system of equations by relating the energy of the observed data to that of the scattered signals.

We will present our algorithm, develop the solution strategy, illustrate performances with numerical examples for both synthetic and real data, and discuss the limitations and advantages of this technique.

ENERGY OF THE WAVEFIELD AND THE BORN APPROXIMATION

We can recover long-wavelength velocity models by solving a system of equations. To derive the equations, we will first review the energy of the wavefield and scattered signals. In signal processing, the energy of a signal x(t) is defined as the zero-lag autocorrelation as (Mitra, 2005; Geldart and Sheriff,

2004)

$$E = \int_0^{t_{max}} u^2(t)dt \quad , \tag{1}$$

where u(t) is the observed wavefield, and t_{max} is the total recording time.

The Born scattering series is derived from the Lippmann-Schwinger integral solution (Ikelle and Amundsen, 2005). This solution requires that we decompose an actual medium into two parts. One part is the background velocity model, and the other is the perturbed model, which is the scattered model. The waves propagating directly from a source to a receiver are called the direct waves or unperturbed waves, and the waves that propagate through scatterers are known as scattered waves or perturbed waves. For a model containing point scatterers, the Lippmann-Schwinger equation enables us to separate the wavefield data as

$$u(t) = u_i(t) + u_p(t) \quad , \tag{2}$$

where u(t) is the acquired wavefield using a source-receiver pair, $u_i(t)$ is the unperturbed components of the wavefield u(t), and $u_p(t)$ is the wavefield components containing the scattered signals.

The scattering can occur at any point in the subsurface, and $u_p(t)$ is approximated by the total sum of the single-point scattered wave signals using the concept of the Born approximation; thus, $u_p(t)$ can be described as

$$u_p(t) \approx \int_\Omega^{t_{max}} s(\mathbf{x},t)d\Omega \quad , \tag{3}$$

where $s(\mathbf{x},t)$ is the 1st-order point-scattered signal, and $\mathbf{x}$ is the position of a scatterer in the subsurface domain Ω. In this study, we assume that $u_i(t)$ contains signals appearing prior to the seafloor reflection, such as a head wave as well as a direct arrival, and does not have the scattered signals from beneath the seafloor. Thus, we can remove it from the data sets.

THE RESPONSES OF POINT SCATTERERS IN A CONSTANT VELOCITY BACKGROUND MODEL

In this study, we cannot use the definition of $s(\mathbf{x},t)$ in eq. (3) for our method due to the computational burden. Our method requires scattered signals from every point in the domain. Computing $u_p(t)$ for a shot demands modeling with the background velocity model and $n_x \times n_z$ modeling procedures, where

n_x and n_z are the numbers of grid points in the x- and z-directions, respectively. Moreover, these modeling procedures must be performed for each source. Therefore, computing $s(\mathbf{x},t)$ is a huge computational burden. Therefore, we designed an approximation of $s(\mathbf{x},t)$ and $\bar{s}(\mathbf{x},t)$.

To define an appropriate function, we empirically investigated the sensitivity of the amplitude of the wavefield to a velocity perturbation using a point scatterer. Fig. 1 shows the signal obtained using a 4th-order finite difference algorithm as a function of velocity perturbation, Δv. The magnitude of the velocity perturbation does not affect the shape of the scattered signal; only its amplitude is affected (Fig. 1b). Fig. 2a shows the value of the peak amplitude of the scattered wavefield as a function of the velocity perturbation,

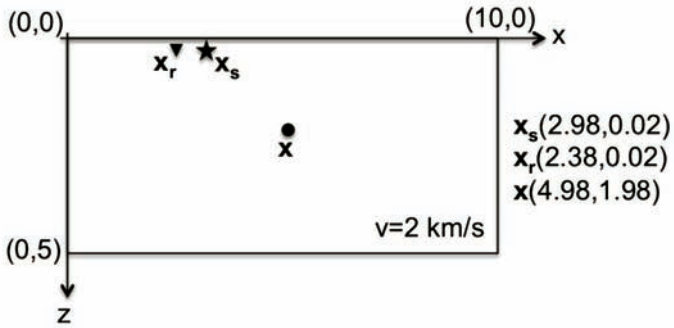

(a)

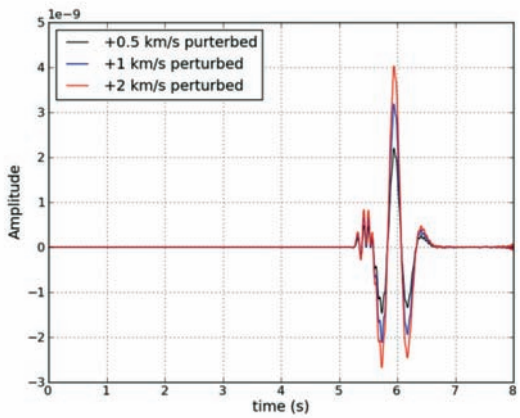

(b)

Fig. 1. (a) The domain of a point-scatter test. The units of the coordinates are in km. (b) Examples of $s(\mathbf{x},t)$ with three different magnitudes of velocity perturbations at the point scatter $\mathbf{x}$.

(a)

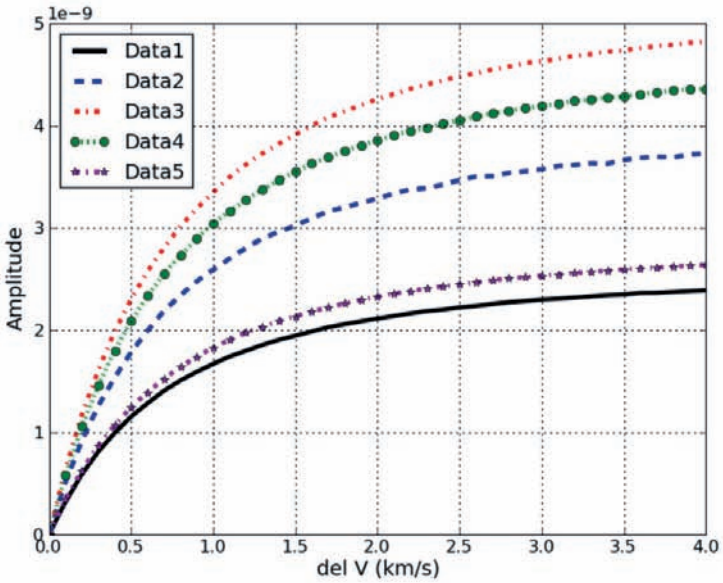

(b)

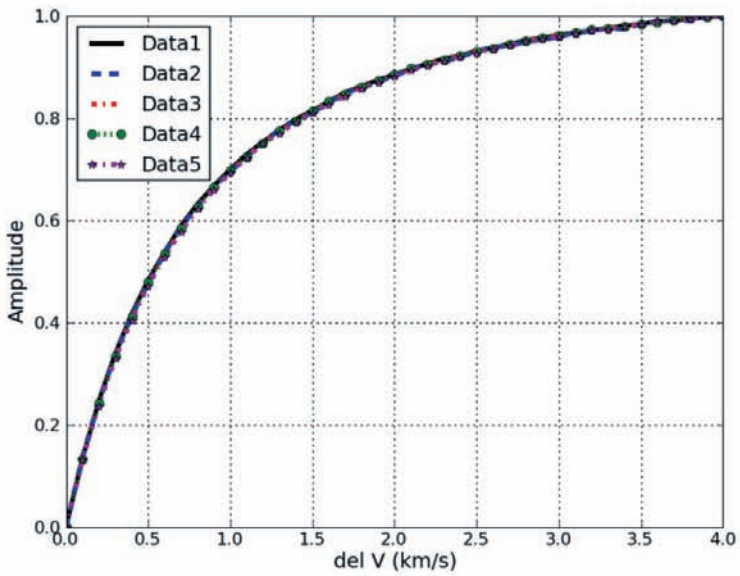

Fig. 2. (a) The result of the test regarding the peak amplitude of the scattered signal versus the perturbed amount of velocity for the five scatters with a different source and receiver position: Data1 [$\mathbf{x}_s$ (12.5 km, 0.05 km), $\mathbf{x}_r$ (3.5 km, 0.05 km), $\mathbf{x}$ (6.25 km, 2.5 km)]; Data2 [$\mathbf{x}_s$ (12.5 km, 0.05 km), $\mathbf{x}_r$ (5.75 km, 0.05 km), $\mathbf{x}$ (12.5 km, 2.5 km)]; Data3 [$\mathbf{x}_s$ (2.5 km, 0.05 km), $\mathbf{x}_r$ (7.75 km, 0.05 km), $\mathbf{x}$ (6.25 km, 7.5 km)]; Data4 [$\mathbf{x}_s$ (6.25 km, 0.05 km), $\mathbf{x}_r$ (12.75 km, 0.05 km), $\mathbf{x}$ (11.25 km, 7.5 km)] and Data5 [$\mathbf{x}_s$ (2.5 km, 0.05 km), $\mathbf{x}_r$ (2.75 km, 0.05 km), $\mathbf{x}$ (2.5 km, 8.75 km)]. (b) The peak amplitude after removing the effect of geometrical spreading. We used this graph as R[Δv].

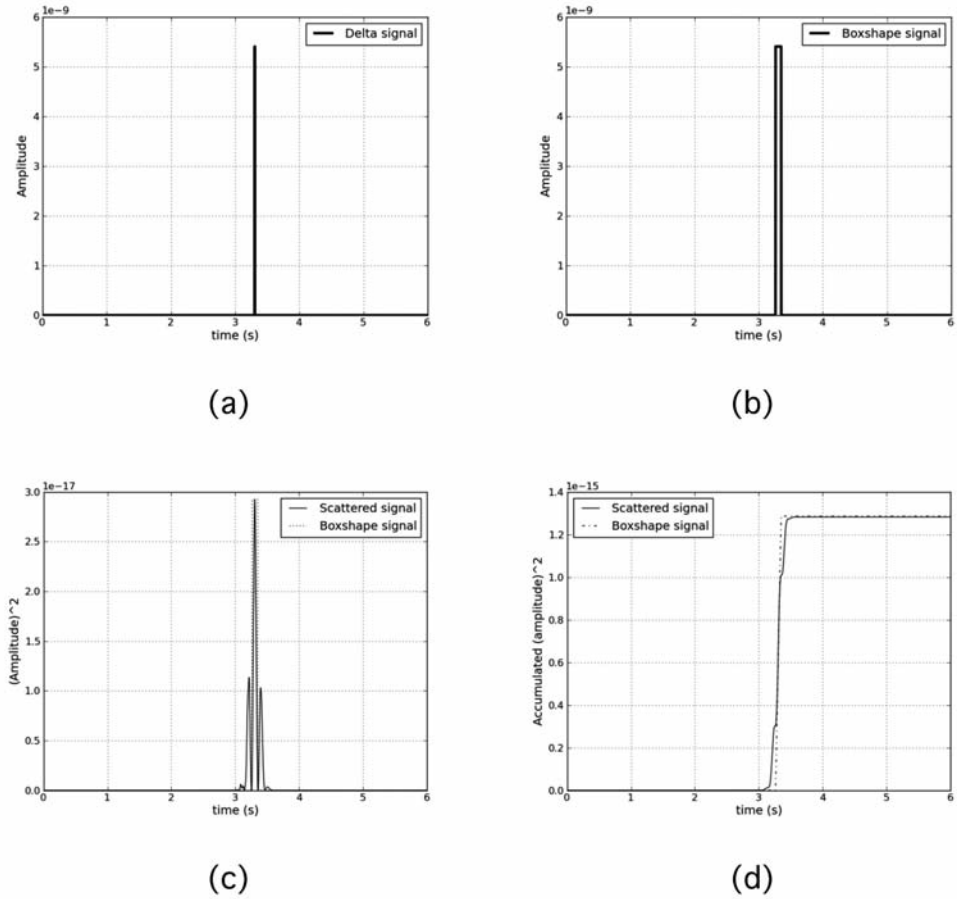

Fig. 3. (a) Delta-function approximation of $\bar{s}(\mathbf{x},t)$. (b) Box-shape approximation of $\bar{s}(\mathbf{x},t)$. (c) The square of the amplitudes of the two data sets are shown in Figs. 1b and 3b with the same perturbation amount, and (d) shows the accumulated square of the amplitudes with time; the value at the maximum time indicates the energy.

Δv, for five scatterers with different source and receiver positions. Then, we normalized each data set to remove the effect of geometrical spreading (Fig. 2b). The resulting peak amplitude, $R[\Delta v]$, is only a function of Δv. From these simple two analyses, we concluded that the amplitude variation of a single point-scattered signal can be decoupled into geometric spreading and a velocity perturbation component, where the effect of geometrical spreading can be calculated analytically (Kuvshinov and Mulder, 2006).

We express $\bar{s}(\mathbf{x},t)$ using this observation as

$$\bar{s}(\mathbf{x},t) = A_0\lambda(\mathbf{x};\mathbf{x}_s)\lambda(\mathbf{x};\mathbf{x}_r)R[\Delta v(\mathbf{x})]\delta(t - t_x) \quad , \tag{4}$$

$$t_x = \mathbf{T}(\mathbf{x},\mathbf{x}_s) + \mathbf{T}(\mathbf{x},\mathbf{x}_r) \quad .$$

where $\mathbf{x}$, $\mathbf{x}_s$ and $\mathbf{x}_r$ are the positions of a point scatterer, source, and receiver, respectively. $\lambda(\mathbf{x}_b;\mathbf{x}_a)$ is the ratio of the amplitude decay during wave propagation from $\mathbf{x}_a$ to $\mathbf{x}_b$ due to geometrical spreading, and $\Delta v(\mathbf{x})$ is the difference between the true velocity and the background velocity model at scattering position $\mathbf{x}$. $R[\Delta v(\mathbf{x})]$ is a function relating the energy scattering ratio and the velocity difference. $\lambda(\mathbf{x}_b;\mathbf{x}_a)$ is calculated by the analytic solution, which will be defined later. $\delta(t - t_x)$ is a delta function. $\mathbf{T}(\mathbf{x},\mathbf{x}_s)$ and $\mathbf{T}(\mathbf{x},\mathbf{x}_r)$ are the traveltimes of the scattered signal from point $\mathbf{x}$ to source $\mathbf{x}_s$ and receiver $\mathbf{x}_r$, respectively. A_0 is the initial amplitude of the source. However, the delta-function signal approximation is not appropriate to express the energy of the scattered signal. We can easily determine that even if the amplitude of the delta function is identical to the perturbed signal's maximum amplitude, the energy of the scattered signal [eq. (1)] cannot be described by the delta-function assumption. Therefore, we change the approximation of the 1st-order point-scattered signal from the delta function to the box-shape signal shown in Fig. 3b and rewrite eq. (4) as

$$\bar{s}(\mathbf{x},t) = A_0\lambda(\mathbf{x};\mathbf{x}_s)\lambda(\mathbf{x};\mathbf{x}_r)R[\Delta v(\mathbf{x})] \quad , (t_x - \varepsilon \le t \le t_x + \varepsilon) \quad . \tag{5}$$

The signal is in the interval between $t_x - \varepsilon$ and $t_x + \varepsilon$ only. Whenever we find the appropriate value of ε, $\bar{s}(\mathbf{x},t)$ can be assumed to have the same energy as $s(\mathbf{x},t)$ for a single point-scattered signal (Figs. 3c and 3d). The selection of the appropriate value of ε will be discussed later.

We redefine eq. (3) using the pseudo 1st-order point-scattered signal $\bar{s}(\mathbf{x},t)$ as

$$u_s(t) \approx \int_{\Omega} \bar{s}(\mathbf{x},t)d\Omega \quad . \tag{6}$$

THE RESPONSE OF POINT SCATTERERS IN A LINEARLY INCREASING BACKGROUND MODEL

During propagation, the amplitude of the signal decreases proportionally to the distance travelled. We selected a linearly increasing velocity model as the background and calculated λ using the amplitude of the analytic solution (Kuvshinov and Mulder, 2006). Additionally, the solution is not a half-space solution, but we use it as an approximation. The analytic solution can be expressed as

$$Amplitude = \lambda(\mathbf{x}_b;\mathbf{x}_a) = 1/\sqrt{[4vv_0\alpha^{-2}(\tilde{u}^2 - 1)]} \quad , \tag{7}$$

where

$$\begin{aligned} \tilde{u} &= 1 + r^2/2\hat{z}_0\hat{z} \quad , \\ \alpha &= (v_{max} - v_0)/z_{max} \quad , \\ \hat{z} &= z + v_0/\alpha \quad , \\ \hat{z}_0 &= z_s + v_0/\alpha \quad , \\ r &= \sqrt{[(x - x_s)^2 + (z - z_s)^2]} \quad , \end{aligned} \tag{8}$$

where v_0 denotes the velocity at the surface, z_{max} is the maximum depth, v_{max} is the velocity at the bottom of the linearly increasing velocity model, $\mathbf{x}_a(x_s,z_s)$ and $\mathbf{x}_b(x,z)$ are the position vectors of the source and receiver, respectively, and r is the distance between the source and receiver.

EQUILIBRIUM EQUATION OF SCATTERING ENERGY

Eq. (6) shows that $u_p(t)$ can be approximated with the total sum of single-scattered wavefields. By the definition of the pseudo 1st-order point-scattered signal and the definition of energy in eq. (1), we can derive the equilibrium equations of the scattering energy at each source and receiver.

$$\int_0^{\bar{t}_{max}} [\int_\Omega \bar{s}(\mathbf{x},t)d\Omega]^2 dt = e^{s,r} \quad . \tag{9}$$

where $e^{s,r}$ is the energy of the signal recorded at r with source s. However, it is difficult to compute the system matrix equation of equation (9), and the exact traveltime is required. To overcome this problem, we assume that the total energy can be approximated by the sum of the energy of each scattered signal. The interference among each scattering signal must not influence the energy distribution of the data to satisfy this assumption. We used a sparse parameterization and the high-frequency approximation, which was shown as a box-shaped signal with a short duration (Fig. 3b), to minimize the interference among the scattered signals. Then, eq. (9) can be rewritten as eq. (10):

$$\int_\Omega \int_0^{t_{max}} \{\bar{s}(\mathbf{x},t)\}^2 dt d\Omega = e^{s,r} \quad . \tag{10}$$

On the right-hand side of eq. (10), the energy is calculated at each receiver position with respect to a shot, which can be calculated from observed wavefield data as

$$e^{s,r} = \int_0^{t_{max}} \{u_p^{s,r}(t)\}^2 dt \quad . \tag{11}$$

We changed the notation $u_p(t)$ to $u_p^{s,r}(t)$ with respect to each source and receiver. Then, we can compute $n_r \times n_s$ scattering energy data. The left-hand side of eq. (10) is derived as follows. First, we consider scattering energy. The energy from a scattering signal is expressed using the definition of energy as

$$\begin{aligned} &\int_0^{t_{max}} \{\bar{s}(\mathbf{x},t)\}^2 dt \\ &= \int_{t_x-\varepsilon}^{t_x+\varepsilon} \{A_0 \lambda(\mathbf{x};\mathbf{x}_s)\lambda(\mathbf{x};\mathbf{x}_r)R[\Delta v(\mathbf{x})]\}^2 dt \\ &= 2\varepsilon A_0^2 \{\lambda(\mathbf{x};\mathbf{x}_s)\lambda(\mathbf{x};\mathbf{x}_r)R[\Delta v(\mathbf{x})]\}^2 \quad , \end{aligned} \tag{12}$$

where time t_x is located at the center of the box signal. We assumed that the amplitude depends on both the distance travelled and $R[\Delta v(\mathbf{x})]$ from eq. (4). The sum of the scattering energy can be expressed as

$$\begin{aligned} &\int_\Omega \int_0^{t_{max}} \{\bar{s}(\mathbf{x},t)\}^2 dt d\Omega \\ &= \int_\Omega 2\varepsilon A_0^2 \{\lambda(\mathbf{x};\mathbf{x}_s)\lambda(\mathbf{x};\mathbf{x}_r)R[\Delta v(\mathbf{x})]\}^2 d\Omega \\ &= 2\varepsilon A_0^2 \int_\Omega \{\lambda(\mathbf{x};\mathbf{x}_s)\lambda(\mathbf{x};\mathbf{x}_r)R[\Delta v(\mathbf{x})]\}^2 d\Omega \quad . \end{aligned} \tag{13}$$

Finally, we build the equilibrium equation of the scattering energy as follows,

$$2\varepsilon A_0^2 \int_\Omega \{\lambda(\mathbf{x};\mathbf{x}_s)\lambda(\mathbf{x};\mathbf{x}_r)R[\Delta v(\mathbf{x})]\}^2 d\Omega = e^{s,r} \quad . \tag{14}$$

If we divide eq. (14) by $2\varepsilon A_0^2$, then we find an interesting characteristic:

$$\int_\Omega \{\lambda(\mathbf{x};\mathbf{x}_s)\lambda(\mathbf{x};\mathbf{x}_r)R[\Delta v(\mathbf{x})]\}^2 d\Omega = e^{s,r}/2\varepsilon A_0^2 \quad . \tag{15}$$

As we mentioned before, adequate selection of ε is important for the validity of our box signal assumption. The value of ε depends on the source signature. If the source signature is invariable for every shot, the value of ε becomes a constant. Therefore, we can ignore ε in this algorithm, which determines the relative ratio of the velocity difference.
Now, we can construct a system of eq. (15) as follows:

$$\mathbf{Kr} = \mathbf{e} \quad , \tag{16}$$

where $\mathbf{K}$ is an $(n_s \times n_r) \times (n_x \times n_z)$ matrix, $\mathbf{r}$ is a vector with $(n_x \times n_z)$ elements, $\mathbf{e}$ is a vector with $(n_s \times n_r)$ elements, and n_s and n_r are the numbers of sources and receivers, respectively. The system can be solved using the normal equation as follows:

$$\begin{aligned} &\mathbf{Kr} = \mathbf{e} \\ &\Rightarrow \mathbf{K}^T\mathbf{Kr} = \mathbf{K}^T\mathbf{e} \\ &\Rightarrow \mathrm{diag}[\mathbf{K}^T\mathbf{K}]\mathbf{r} = \mathbf{K}^T\mathbf{e} \\ &\Rightarrow \mathbf{r} = \mathbf{K}^T\mathbf{e}/\mathrm{diag}[\mathbf{K}^T\mathbf{K}] \quad . \end{aligned} \tag{17}$$

We calculate $\mathbf{r}$ using diagonal components only because of the limitation of computational resources. By only using diagonal components, our algorithm becomes extremely fast and inexpensive. Then, we can compute the anomaly $\mathbf{r}$, which is a relative ratio, and can show where the velocity anomaly is located. However, we cannot obtain a negative value of $\mathbf{r}$ because only the diagonal of the matrix is used.

THE SCALING AND UPDATING METHOD

We test our algorithm with the Pluto model (Stoughton et al., 2001), as shown in Fig. 4a. We can calculate the velocity anomaly ratio, $\Delta v(\mathbf{x})$, using $\mathbf{r}(\mathbf{x}) = R[\Delta v(\mathbf{x})]^2$ and the graph shown in Fig. 2b. The computed anomaly $\mathbf{r}(\mathbf{x})$ is shown in Fig. 7b, which shows where the high-velocity structure is. However, the result is very smooth and has a wide spread. The position of the maximum value in our result may be an accurate position of the structure, but the surrounding region that contains high-velocity structures also has large values. By inspection, we believe that it is more suitable to curtail the range of the result with a scaling method. We can control the size of anomalous bodies with the following scheme:

$$\Delta v_{after} = N\left|(\Delta v_{before})^q\right| \quad , \tag{18}$$

where $N|\cdot|$ is the normalized value of $\cdot$, and q is a scaling constant. In this scheme, as the value of q becomes larger, the size of the anomalous bodies becomes smaller. In this study, we used $q = 2$. From this procedure, we can obtain more reasonable results for velocity updating, as shown in Fig. 7c.

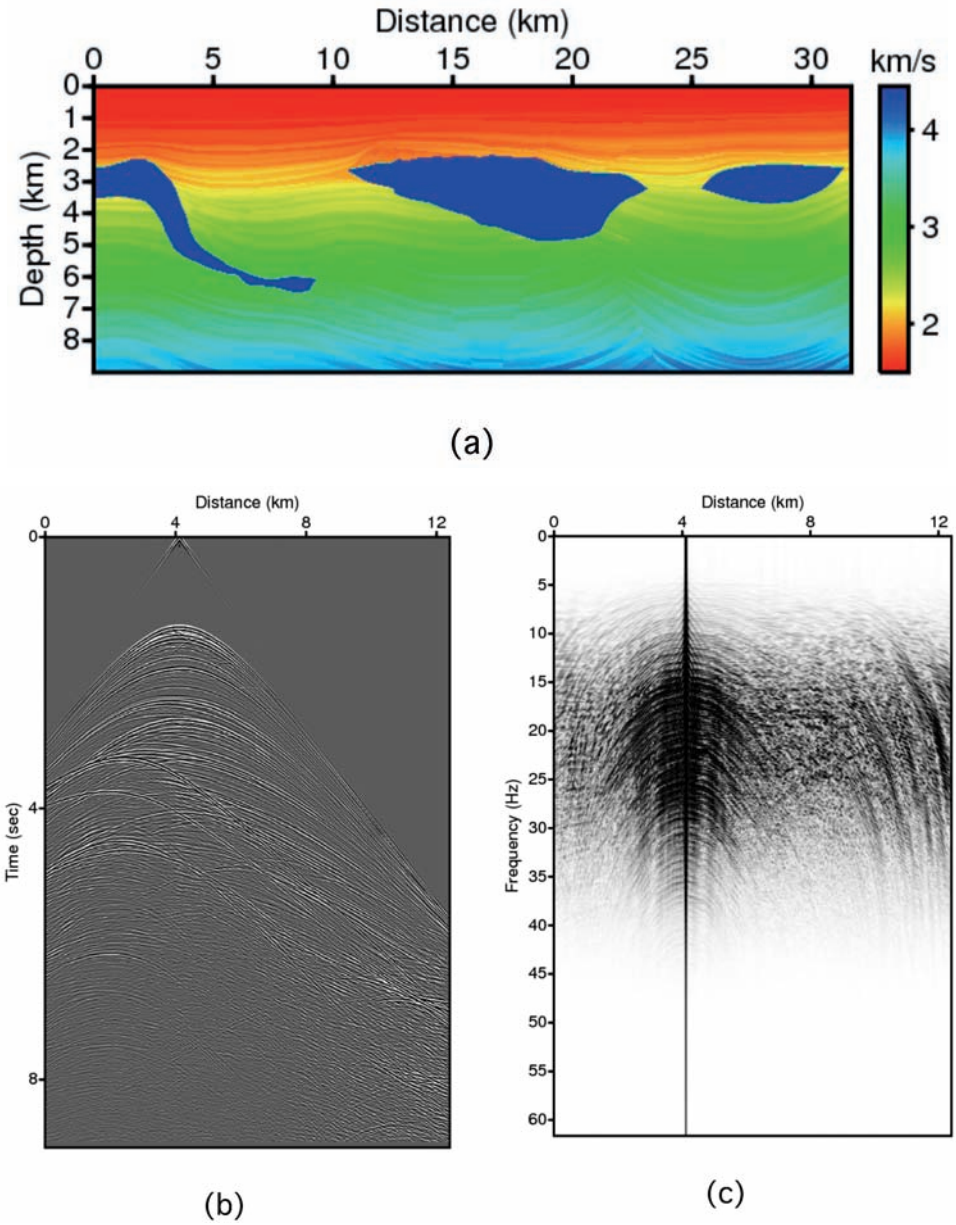

Fig. 4. (a) The Pluto velocity model, (b) a shot gather, and (c) the frequency spectrum of the shot gather.

In this algorithm, we compute the velocity model by updating the initial velocity with a scaled anomaly as follows:

$$v_r(\mathbf{x}) = v_0(\mathbf{x}) + \gamma \Delta v(\mathbf{x}) \quad , \tag{19}$$

where $v_r(\mathbf{x})$ is the computed velocity by our algorithm, $v_0(\mathbf{x})$ is the initial velocity, and γ is a step length for the update. To determine a proper q and γ, we performed several line searches that calculated the error between the seismograms obtained using the actual and computed velocity models.

SYNTHETIC DATA EXAMPLES

Pluto model

We tested our algorithm with seismograms from the Pluto 1.5 dataset shown in Fig. 4, which has been generated by the SMAART Joint Venture Consortium (Stoughton et al., 2001). Its seismograms were computed using a 4th-order finite difference modeling program in the time domain. There were 1,387 shots and 540 receivers for each shot, and the maximum recording time was 9 s with a sampling interval of 8 ms. The maximum offset was 8.229 km (27,000 ft) behind a shot and 3.962 km (13,000 ft) ahead of a shot. The Ricker wavelet was used as the source wavelet. Good results are difficult to obtain with the Pluto dataset using a conventional full waveform inversion or migration without a proper initial velocity model. The existence of multiples and the absence of low-frequency components hinder the construction of a reliable velocity model. Fig. 5 shows a frequency-domain full waveform inversion and a migration result that began with a linearly increasing starting velocity model (Fig. 7a). The result of the inversion does not show the high-velocity structures (Fig. 5a). Furthermore, the migration image shows only the top of the high-velocity structures, as shown in Fig. 5b.

Fig. 6 shows the split shot gather and the scattering energy for the new algorithm. For our test, we used a linearly increasing velocity model, from 1.5 km/s to 4.0 km/s, as the initial model (Fig. 7a). We fixed the velocity of the water layer and calculated the velocity below a sea bottom by dividing the model by 23 $\times$ 23 m blocks. Fig. 7b and c shows the velocity anomaly ratio and the scaled anomaly data for updating. Compared with the Pluto model, we know that the positions of the anomalies are in good agreement with the actual model (Fig. 7d). We updated the initial velocity using the velocity differences (Fig. 7c), and then we recovered a macro-velocity model using the scaling scheme (Fig. 7e).

We also performed a full waveform inversion and migration with the computed velocity model as an initial velocity model for a comparison with the

case of the linearly increasing initial velocity model. In contrast to the previous result that began with the linearly increasing velocity model, the inversion that began from our computed velocity model yielded a reliable result (Fig. 8a) that shows the shape of the high-velocity structure. The migration image (Fig. 8b) shows not only the top boundaries but also the bottom boundaries of the high-velocity structures.

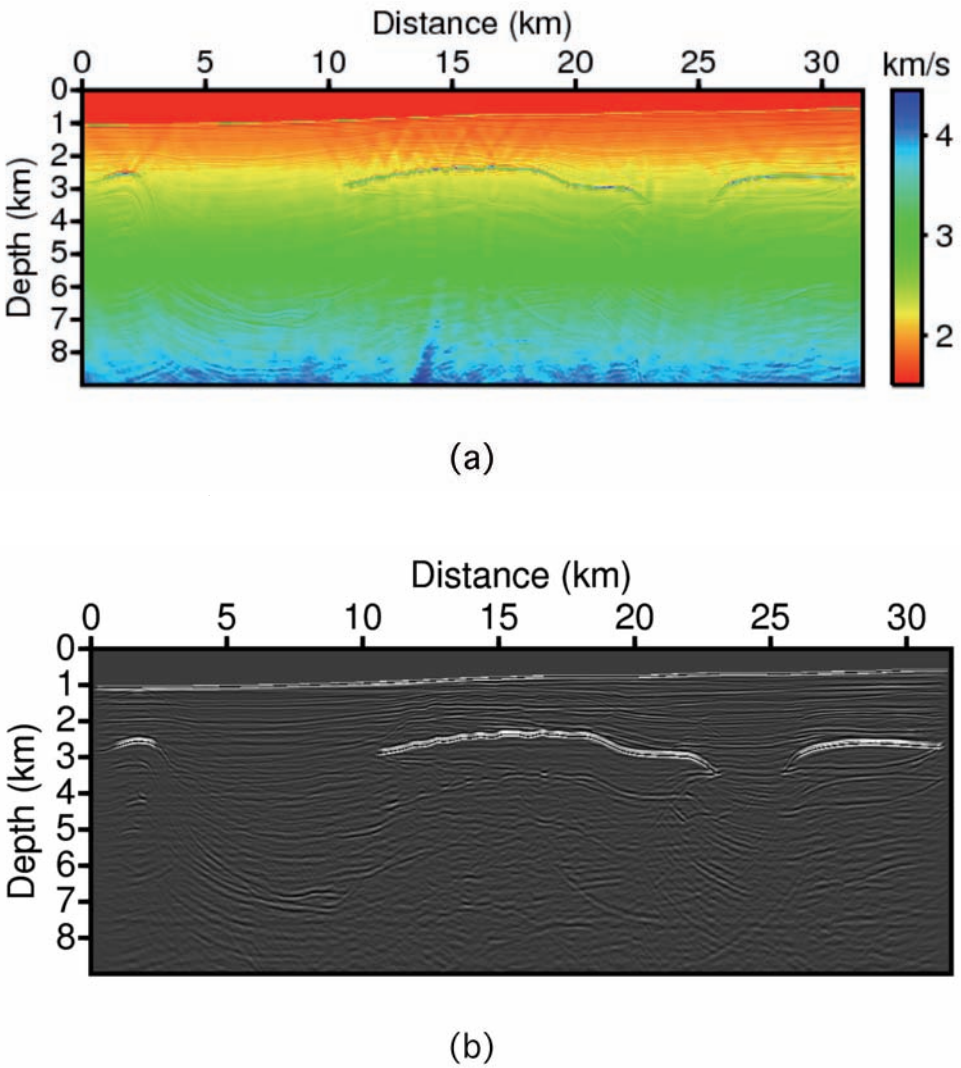

Fig. 5. (a) The inverted velocity model at the 100-th iteration using a linearly increasing velocity model whose velocity increased from 1.5 km/s to 4.0 km/s as an initial model by a frequency domain full waveform inversion. (b) Migration images obtained using the inverted velocity model shown in Fig. 5a.

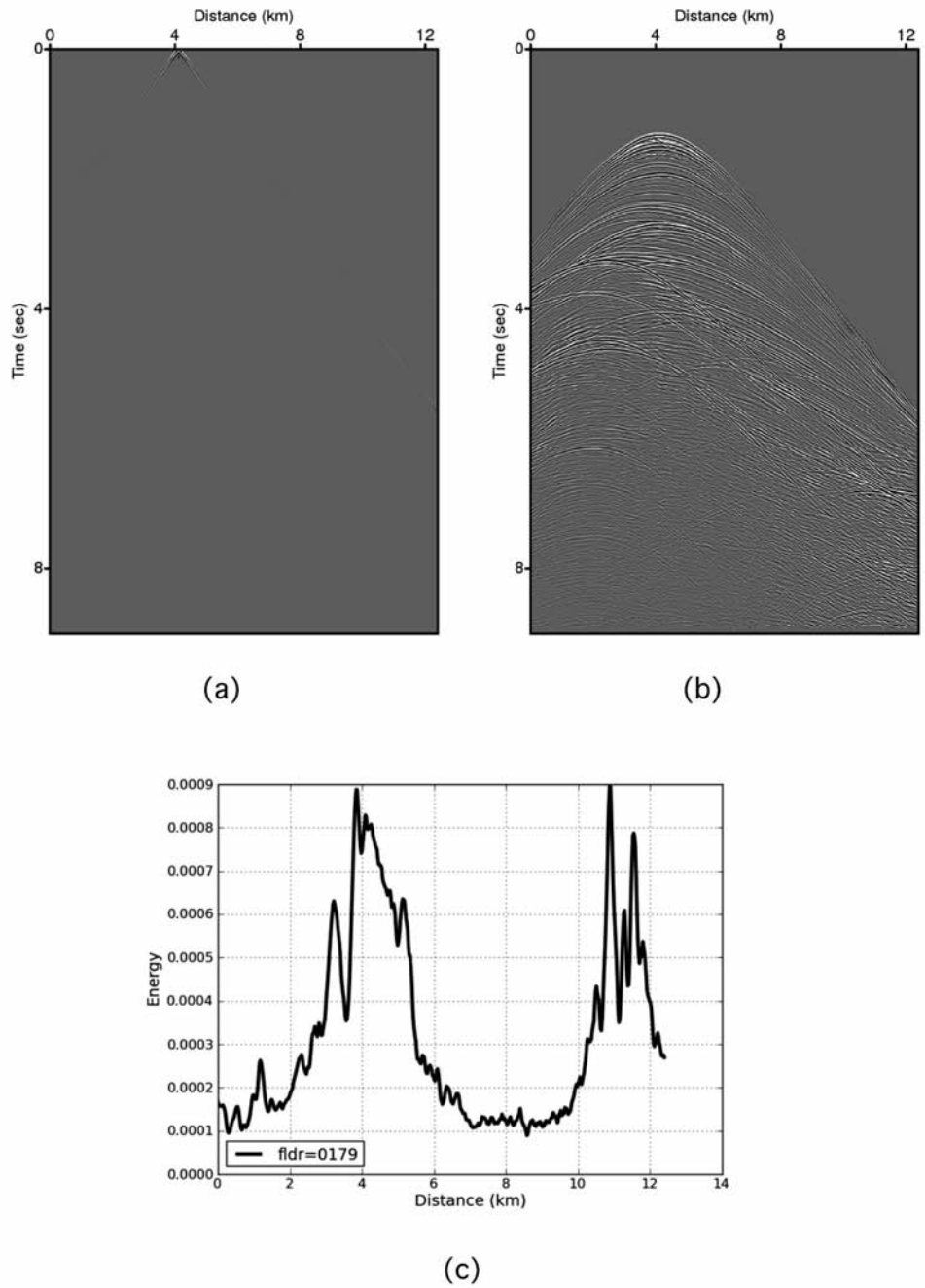

Fig. 6. A common shot gather from the model shown in Fig. 4a decomposed into the (a) incident wavefield u_i and (b) the scattered wavefield u_p. (c) The energy of each trace of u_p.

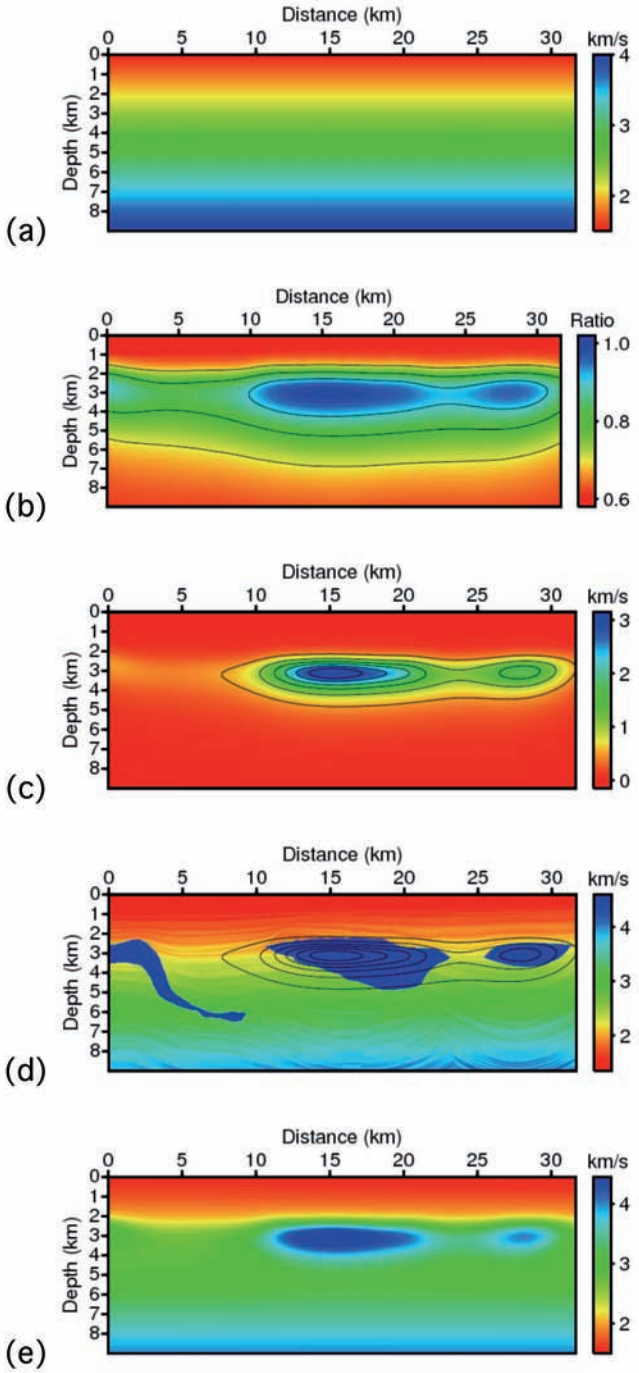

Fig. 7. Velocity models. (a) The initial velocity model, (b) the computed anomaly, $\mathbf{r}(\mathbf{x})$, (c) the scaled velocity anomaly, (d) the Pluto velocity model superimposed on the contour of the velocity anomaly, and (e) the computed velocity model from our algorithm.

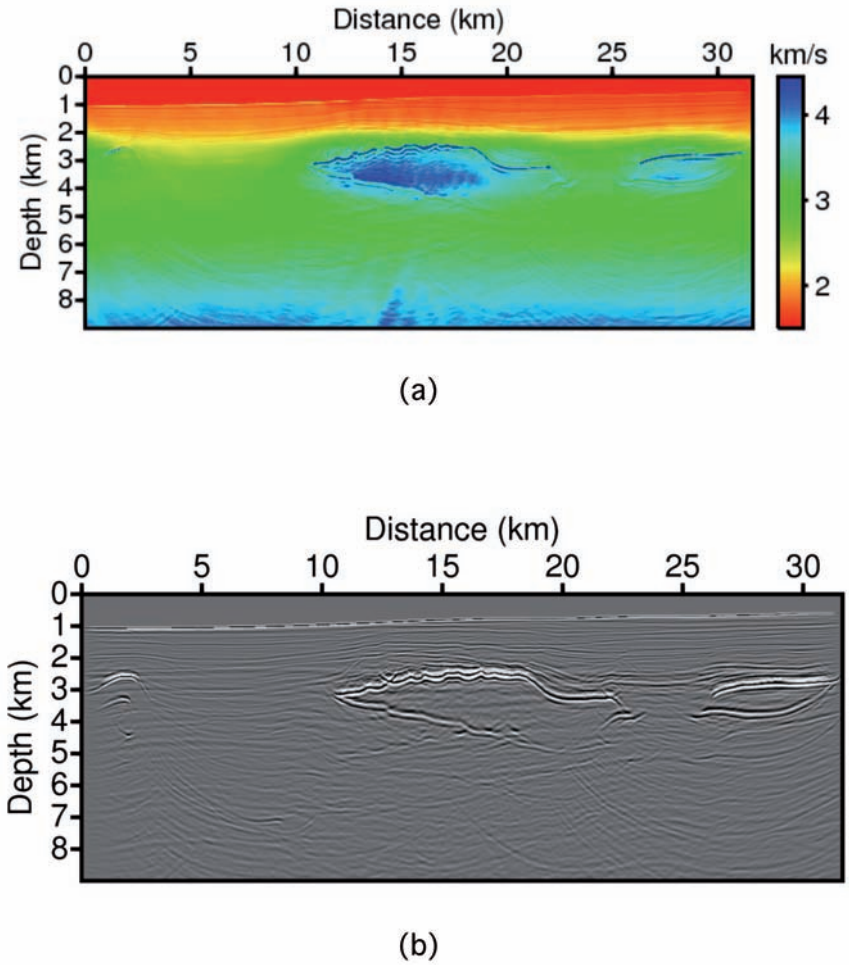

Fig. 8. (a) The inverted velocity models at the 100-th iteration using the computed velocity model (Fig. 7e) as an initial model by a frequency-domain full waveform inversion. (b) Migration images obtained using the inverted velocity model shown in Fig. 8a.

BP model

We also tested the algorithm with the BP data set (Billette and Brandsberg-Dahl, 2005). The BP velocity model is 67 km long and 12 km deep (Fig. 9a). The data were generated with a streamer configuration using a 15-km streamer with 12.5-m group intervals and 50-m shot intervals. The number of sources was 1,340, and each source had 1,201 receivers. Fig. 9b shows a shot gather. The data were recorded for 12 s with a 6 ms sampling interval. The dominant frequency of the data is 25 Hz, and there are a small amount of low-frequency components in the data, as shown in Fig. 9c.

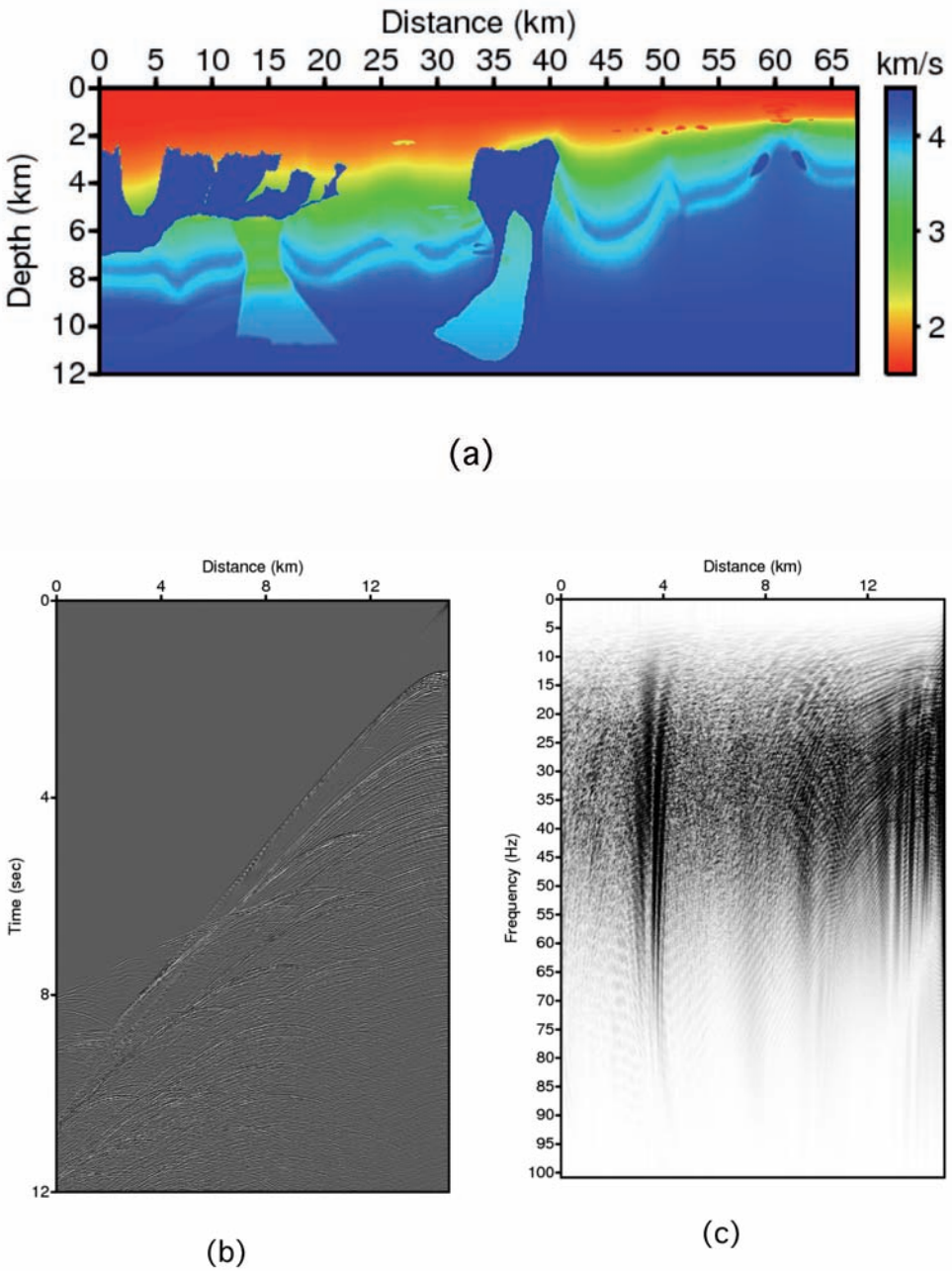

Fig. 9. (a) The BP velocity model, (b) a shot gather, and (c) the frequency spectrum of the shot gather.

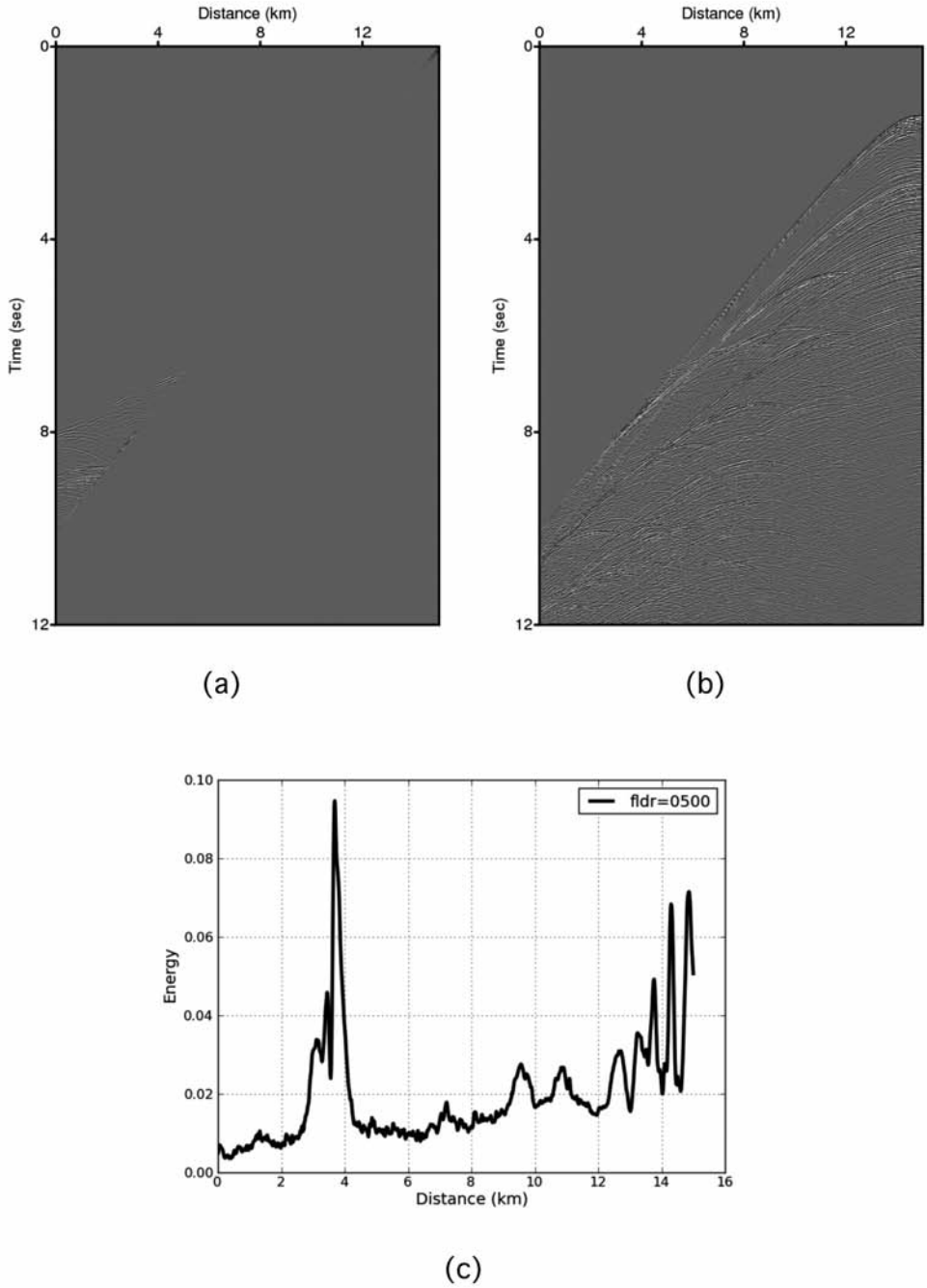

Fig. 10. A common shot gather from the model shown in Fig. 9a decomposed into (a) the incident wavefield u_i and (b) the scattered wavefield u_p. (c) The energy of each trace of u_p.

Fig. 10 shows the u_i and u_s parts of the data for a shot gather and its scattering energy. The test began with a linearly increasing velocity model; the velocity of this model varied from 1.5 km/s to 4.5 km/s (Fig. 11a). We calculated the relative velocity anomalies using the energy of the data set and the energy of the pseudo-scattered signals from the initial model. Fig. 11b shows the result of this calculation. The relative anomalies show the location of the high-velocity structures. Fig. 11c shows the computed velocity anomaly for the velocity update. We displayed the contour image with the BP model to verify the location of the anomalies, as shown in Fig. 11d. Finally, we obtained a macro-velocity model (Fig. 11e). In the update process, we constrained the maximum velocity to 4.5 km/s.

FIELD DATA TEST

We tested our algorithm using field data from TGS-NOPEC (Fig. 12). The data were acquired in an ultra-deep water environment where the average sea depth is approximately 2 km. There were 1,334 shots, and each shot had 320 receivers. The minimum offset distance was 147 m, and the maximum offset distance was 8,122 m. The total recording time was 14.3 s with a sampling rate of 4 ms. We used a linearly increasing velocity model, whose velocity varied from 1.5 km/s to 3.0 km/s, as the background velocity model.

Fig. 13a shows the result of our algorithm using the data set, and Fig. 13b shows the result of the full waveform inversion in the frequency domain using the computed velocity model as an initial velocity model. With the full waveform inversion in the frequency domain, the resolution of the coarse-scaled velocity model improved. The inverted velocity model (Fig. 13b) shows high-velocity structures in the subsurface with improved resolution. To verify the inverted velocity model, we obtained a reverse time migration from this model, as shown in Fig. 13c. The image clearly shows the subsurface layers and structures.

DISCUSSION

To examine the effect of the lack of low frequencies in the proposed algorithm, we applied a bandpass filter, as shown in Fig. 14a, to the Pluto data (Fig. 4b). Fig. 14b shows the scattering energy distribution of the original data and the filtered data. The energy distribution of the filtered data shows more high-wavenumber features compared with the original distribution. Although we removed the low-frequency information, the general trend of the energy distribution of the filtered data is similar to the original distribution. Fig. 15 shows the inversion results of both the original data and the filtered data. Note that the results of both data sets are very similar to each other, which shows the robustness of the algorithm with respect to the lack of low-frequency content in the data.

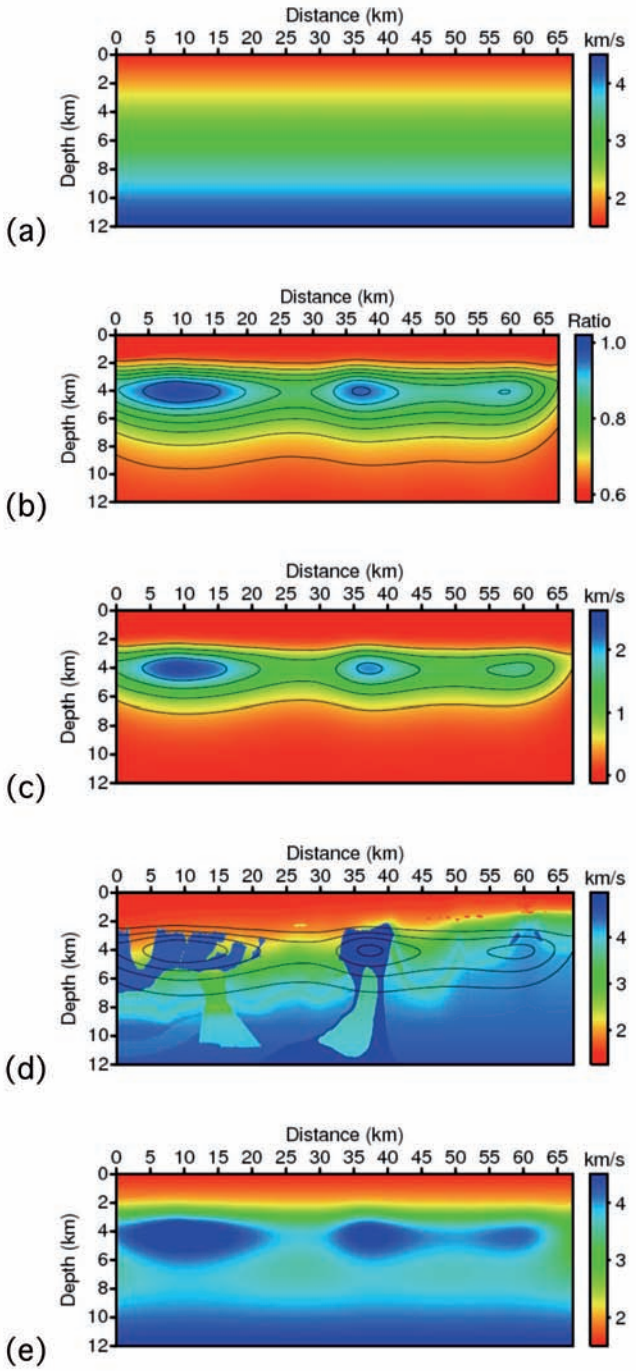

Fig. 11. Velocity models. (a) The initial velocity model, (b) the computed anomaly, , (c) the scaled velocity anomaly, $\mathbf{r}(\mathbf{x})$, (d) the BP velocity model with the contour of the scaled velocity anomaly, and (e) the computed velocity model from our algorithm.

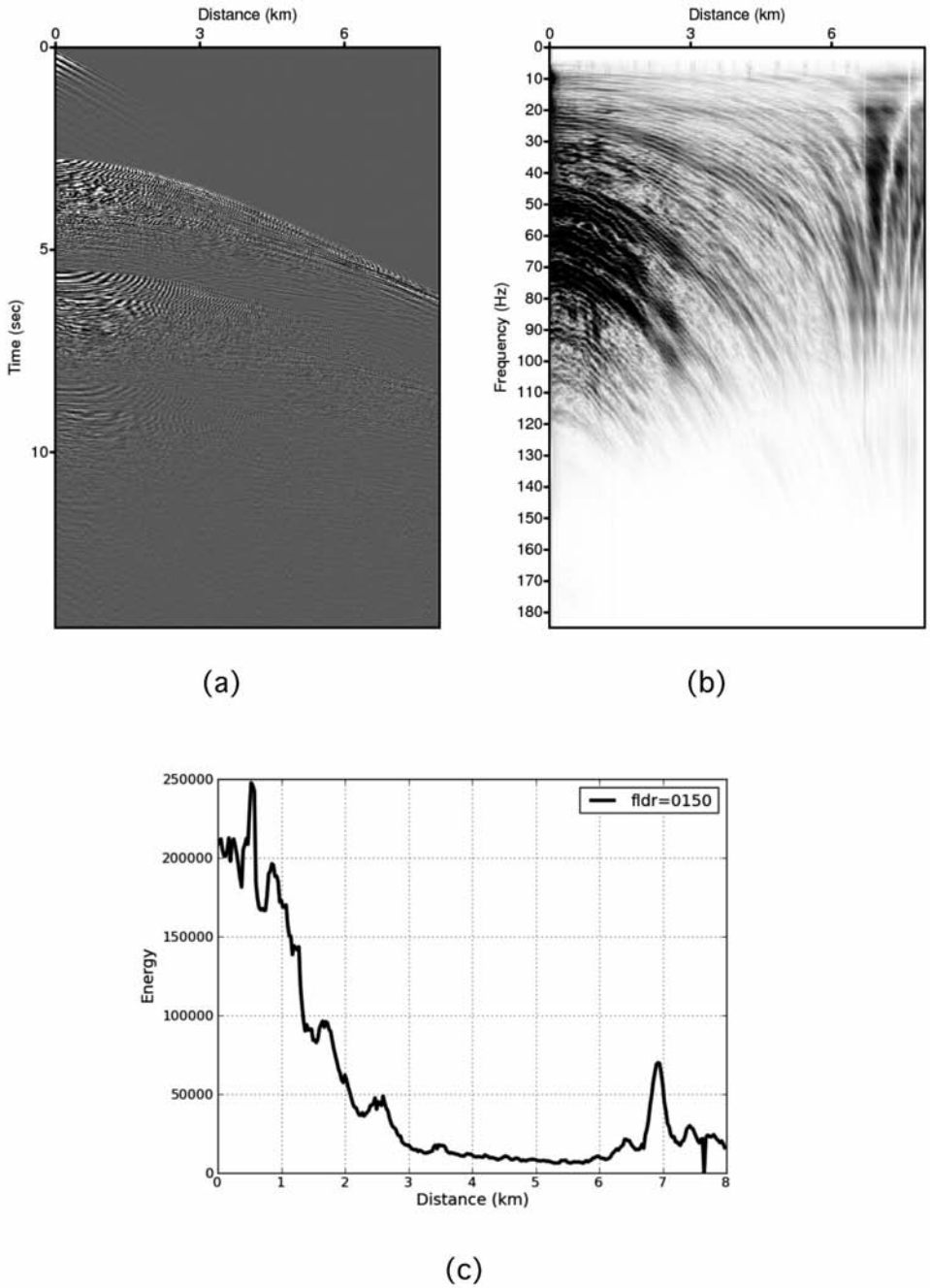

Fig. 12. (a) A shot gather of the TGS-NOPEC data set, (b) the frequency spectrum of the shot gather and (c) the converted energy.

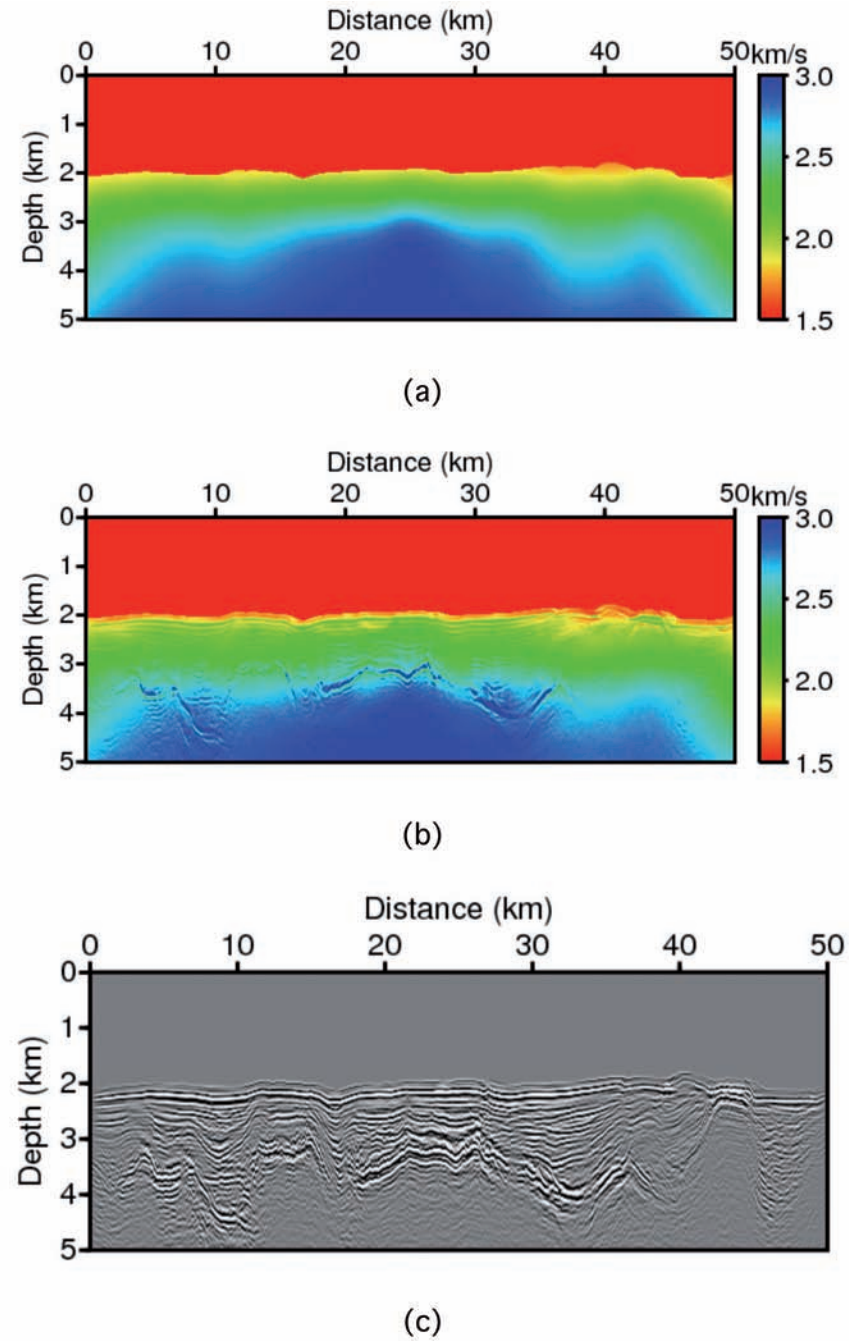

Fig. 13. (a) The computed velocity model using the TGS-NOPEC data set, (b) the inverted velocity model at the 100-th iteration using the computed velocity model as an initial velocity model with the frequency domain FWI, and (c) the migration images using the inverted velocity model shown in Fig. 13b.

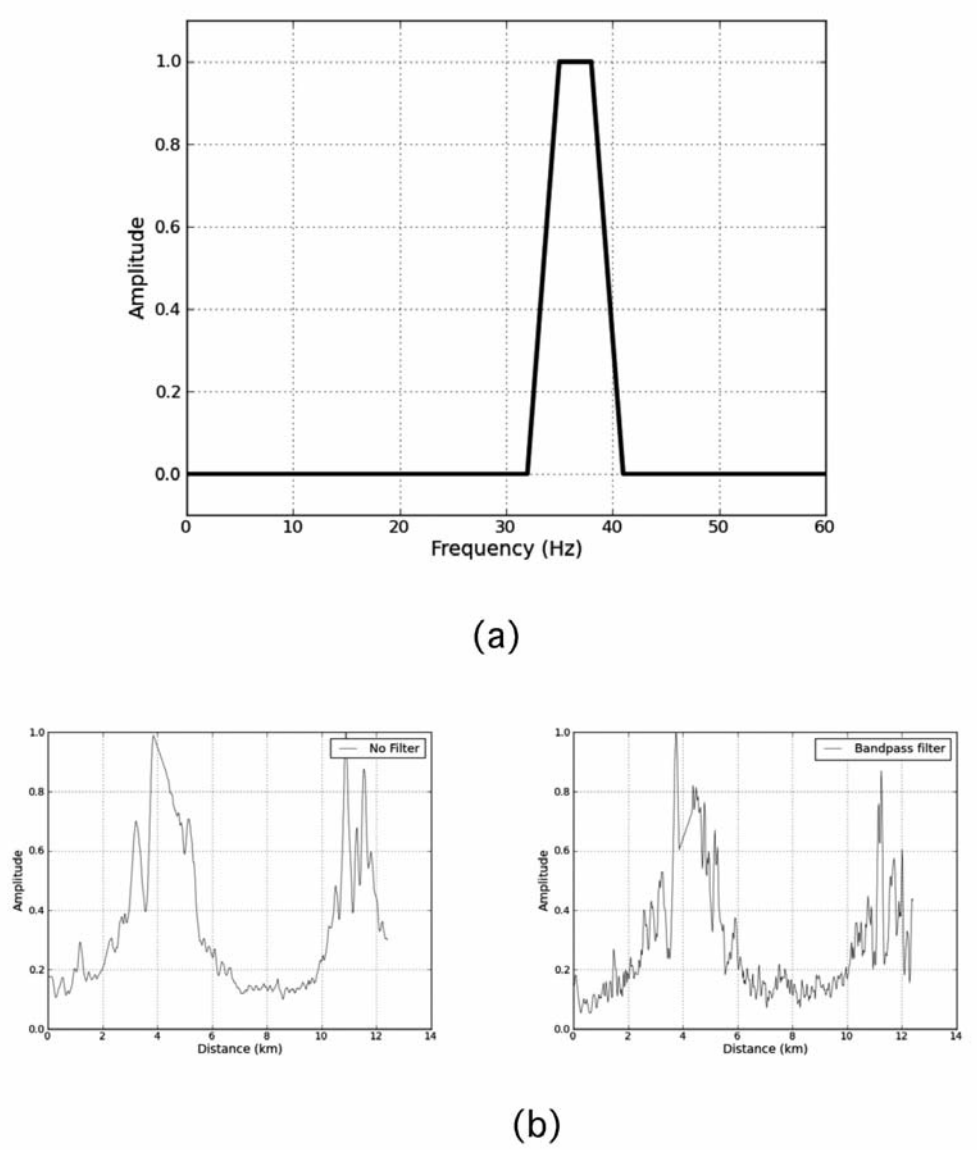

Fig. 14. (a) The illustration of the band-pass filter. (b) The energy distributions of the original data and the filtered data.

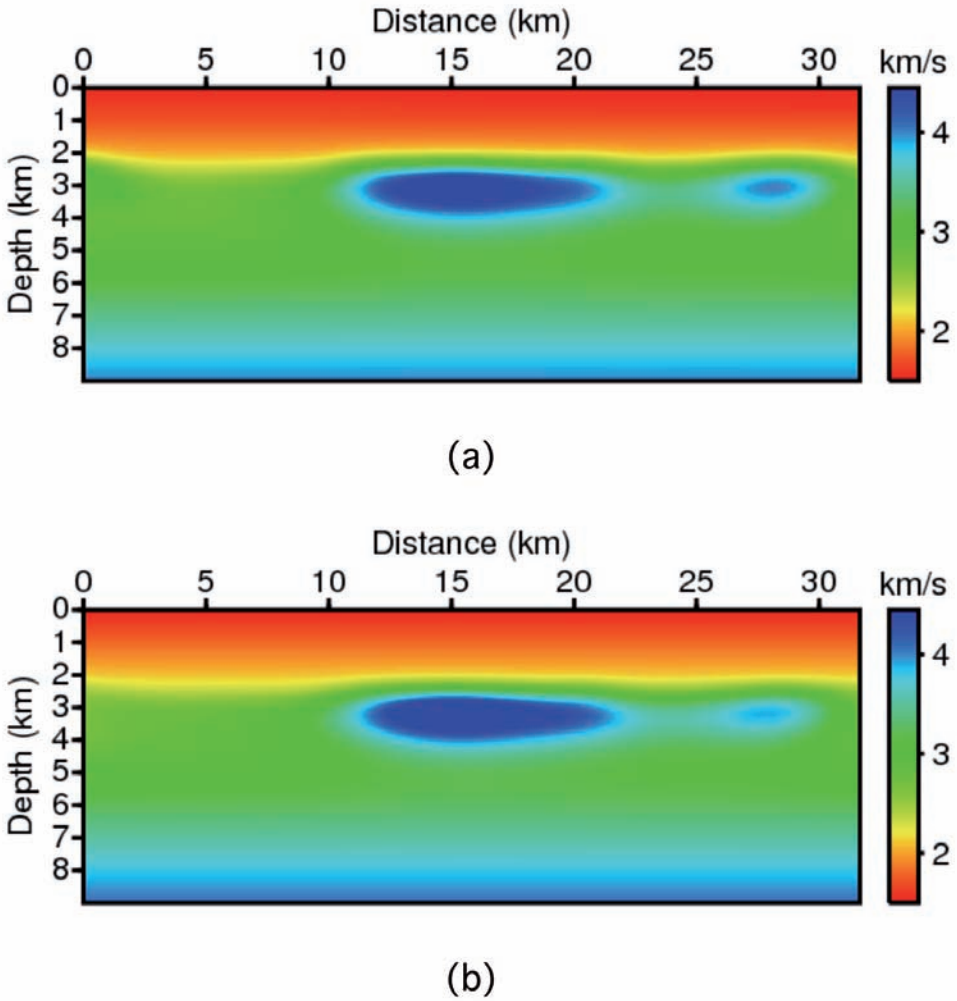

Fig. 15. The computed coarse-scale velocity models using (a) the original data (Fig. 7e) and (b) the filtered data (Fig. 14).

While deriving the matrix equation [eq. (17)], we ignored interferences among the scattered signals. Although we used box-shaped signals and sparse parameterizations to minimize the interferences, this approximation introduces errors in the energy distribution calculation. Moreover, the pseudo-scattered signal approximation is also a source of error. Accordingly, the proposed method does not recover all the anomalies in the subsurface. For example, the computed model (Fig. 11e) does not show the inclined high velocity at the bottom right of the BP model. We found that our method only recovers structures generating large energy. We believe that this recovery was also related to the $R[\Delta v]$ obtained by the empirical method. Furthermore, using positive diagonal components of the matrix ensures that our method recovers only the high-velocity anomalies compared with an initial velocity model. Although many approximations were introduced, the proposed method resulted in accurate macro-velocity models. These models can serve as an accurate initial velocity model for subsequent processes, as shown in the numerical examples.

Using this energy data, the total amount of data was reduced from $n_s \times n_r \times n_t$ to $n_s \times n_r$, which means that the resolution of an inversion result is reduced when compared with other schemes using all the data. In contrast, we efficiently obtained macro-velocities using the pseudo-scattered signal. For example, the computation for the Pluto model shown in Fig. 7 required 194.2 s using five 2.26-GHz CPUs.

CONCLUSION

We proposed a new method to find a macro-velocity model inspired by the idea of gravity inversion, the Born approximation, and the energy of seismic data. We excluded the direct wave and the head wave to compute the energy of the scattered data. The energy profiles appear similar to a gravity anomaly, and the inverted velocity appears similar to the results of the gravity inversion in many respects.

The robustness of this method was shown by numerical examples, including examples with field data. We showed that this algorithm yields macro-velocity models. The macro-velocity model using our algorithm is acceptable as an initial velocity model for a subsequent full waveform inversion. The new scheme can be used with real data that does not contain low-frequency contents to build a macro-velocity model for full waveform inversion or migration. The proposed method requires further studies that investigate the reliable scaling factor, the step-length constant and a technique to delineate low-velocity regions below a high-velocity area.

ACKNOWLEDGMENT

This work was supported financially by the Energy Efficiency & Resources (No. 2010T100200376) and Human Resources Development program (No. 20124010203200) of the Korea Institute of Energy Technology Evaluation and Planning (KETEP) grant funded by the Korea government Ministry of Knowledge Economy.

REFERENCES

Billette, F.J. and Brandsberg-Dhal, S., 2005. The 2004 BP Velocity Benchmark. Extended Abstr., 67th EAGE Conf., Madrid: B035.

Chapman, C.H. and Pratt, R.G., 1992. Traveltime tomography in anisotropic media - I. Theory. Geophys. J. Internat., 109: 1-19.

Geldart, L.P. and Sheriff, R.E., 2004. Problems in Exploration Seismology and their Solutions. SEG, Tulsa, OK. ISBN 1560801158.

Guspi, F., 1993. Noniterative nonlinear gravity inversion. Geophysics, 58: 935-940.

Ikelle, L.T. and Amundsen, L., 2005. Introduction to Petroleum Seismology. SEG, Tulsa, OK. ISBN 1560801298.

Kuvshinov, B.N. and Mulder, W.A., 2006. The exact solution of the time-harmonic wave equation for a linear velocity profile. Geophys. J. Internat., 167: 659-662.

Last, B.J. and Kubik, K., 1983. Compact gravity inversion. Geophysics, 48: 713-721.

Luo, Y. and Schuster, G.T. 1991. Wave-equation traveltime inversion. Geophysics 56, 645-653.

Mitra, S.K. 2005. Digital signal processing: A computer-based approach. McGraw-Hill College. ISBN 0073048372

Shin, C. and Cha, Y.H., 2008. Waveform inversion in the Laplace domain. Geophys. J. Internat., 173: 922-931.

Shin, C. and Ha, W., 2008. A comparison between the behavior of objective functions for waveform inversion in the frequency and Laplace domains. Geophysics, 73: VE119-VE133.

Stoughton, D., Stefani, J. and Michell, S., 2001. 2D elastic model for wavefield investigations of subsalt objectives, deep water Gulf of Mexico. Expanded Abstr., 71st Ann. Internat. SEG Mtg., San Antonio: 1269-1272.